Experiments in Fluids 37 (2004) 825–833
DOI 10.1007/s00348-004-0870-7

Near-surface velocimetry using evanescent wave illumination

S. Jin, P. Huang, J. Park, J.Y. Yoo, K.S. Breuer

Abstract Total internal reflection velocimetry (TIRV) is used to measure particle motion in the near-wall region of a microfluidic system. TIRV images are illuminated with the evanescent field of an incident laser pulse and contain only particles that are very close to the channel surface. Sub-micron-sized fluorescent particles suspended in water are used as seed particles and their images are analyzed with a particle tracking velocimetry (PTV) algorithm to extract information about apparent slip velocity. At relatively low shear rates (less than 2,500 s^{-1}), a velocity proportional to the shear rate was observed. The statistical difference between velocities measured over hydrophilic and hydrophobic surfaces was found to be minimal. The results suggest that the slip length, if present, is less than 10 nm, but uncertainty regarding the exact character of the illumination field prevents a more accurate measurement at this time. Numerical simulations are presented to help understand the results and to provide insight into the mechanisms that result in the experimentally observed distributions. Issues associated with the accuracy of the experimental technique and the interpretations of the experimental results are also discussed.

A version of this paper was presented at the 5th international symposium on particle image velocimetry (PIV 2003), Busan, Korea, 22–24 September 2003.

Received: 12 November 2003 / Accepted: 11 August 2004
Published online: 23 October 2004

P. Huang, K.S. Breuer (✉)
Division of Engineering, Brown University, Providence, Rhode Island 02912, USA
E-mail: kbreuer@brown.edu

S. Jin, J.Y. Yoo
School of Mechanical and Aerospace Engineering, Seoul National University, Seoul, 151-742, Korea

J. Park
Division of Mechanical Engineering, Ajou University, Gyeonggi, 443-749, Korea

The authors would like to thank Thomas Powers for his discussion on issues regarding the simulation of Brownian motion in shear flow; Min-Jun Kim for assistance in channel fabrication, and the rest of the Brown University Microfluidics Lab for their support. Two authors (SJ and JYY) acknowledge support from the Brain Korea 21 Project and the Micro Thermal System Research Center, Seoul National University.

1 Introduction

Over the past few years, studies regarding near-wall fluid motion have intensified because of the emergence of micro-electro-mechanical-systems (MEMS), where the fluid–surface interaction is important to the design, fabrication, and performance of these devices. In particular, the no-slip boundary condition, which has long been experimentally verified in macroscopic flow, now receives a great deal of attention in microfluidics. Moreover, many biological applications of microfluidic devices require surface coatings that change the wetting ability of aqueous or biological fluids. Thus, a better understanding of fluid–surface interaction becomes necessary in designing applicable devices.

Many experimental techniques have been applied to study the effect of slip on both hydrophilic and hydrophobic surfaces. In general, slip measurement techniques can be classified into indirect and direct methods. In the indirect methods, slip velocity is inferred from other measurements, for example, the flow rate and pressure within the flow duct (Schnell 1956; Churaev et al. 1984; Choi et al. 2003), or from forces required to move the surfaces (Zhu and Granick 2002). Examples of the direct measurement methods include hot film anemometry (Watanabe et al. 1999), total internal reflection fluorescence recovery after photobleaching (FRAP) (Pit et al. 2000), and micro-PIV (Tretheway and Meinhart 2002). There are also other groups of researchers who attempted to understand the slip phenomenon from a theoretical perspective through molecular dynamics simulations (Thompson and Troian 1997; Barrat and Bocquet 1999; Cieplak et al. 2001). The results from these studies are quite diverse, and *apparent slip* lengths ranging from nanometers to microns have been reported. Similarly, the dependence of the slip on the applied shear rate is also a matter of debate, with some results suggesting a constant slip length, while others reporting a slip length dependent on shear rate and/or surface hydrophobicity.

Recently, a novel technique termed total internal reflection fluorescence microscopy (TIRFM) has been applied to near-wall fluid measurements. The TIRFM technique has long been used in biological studies, such as cell-substrate contacts, vesicle fusion, and single-molecule observation (Thompson and Langerholm 1997; Burmeister et al. 1998; Toomre and Manstein 2001). It takes advantage of the fact that total internal reflection occurs when light travels from a dense medium (such as a glass cover slip) with refractive index n_1 into a less dense medium (such as

the sample fluid) with refractive index n_2. Total internal reflection occurs if the incident angle is larger than the critical angle $\theta_c=\sin^{-1}(n_2/n_1)$, which can be derived from Snell's Law. When total internal reflection occurs, some fraction of the light energy penetrates into the less dense medium and propagates parallel to the surface. This parallel light wave is known as the *evanescent wave*. One characteristic of the evanescent wave is that its intensity I decays exponentially with respect to the distance from the two-media interface. Thus, images taken under evanescent wave illumination have low background noise, showing clear features of sample structure that is near the interface. There have also been several recent experimental studies of fluid mechanics by applying evanescent wave illumination (Yamada 1999; Pit et al. 2000; Zettner and Yoda 2003). In particular, Zettner and Yoda (2003) used the particle image velocimetry (PIV) technique combined with evanescent wave illumination to measure the near-surface velocity field in rotating Couette flow.

In this paper, we describe the total internal reflection velocimetry (TIRV) technique, in which the TIRFM technique is applied to observe particle motion in the close vicinity of microchannel walls with different surface wetting properties. A particle tracking velocimetry (PTV) technique is applied to track particle displacements and flow velocities near the wall.

2 Experimental procedures

The TIRFM technique requires the creation of total internal reflection of a laser beam at the glass–sample interface, and the presence of fluorescent molecules or particles suspended in the sample fluid for imaging and measurement. Two different optical configurations are commonly used to create an evanescent field close to the glass–sample interface. The first method utilizes a prism to guide the laser beam into the glass cover slip, which then serves as a waveguide, allowing total internal reflection to occur. The other method, which is prismless, has the illuminating laser beam directed through a high numerical aperture (*NA*) microscope objective at an angle that creates total internal reflection at the glass–sample interface, as shown in Fig. 1. The maximum incident angle which can be achieved by using an objective lens is given by:

$$\theta_{\max} = \sin^{-1}\left(\frac{NA}{n_{\text{glass}}}\right) \tag{1}$$

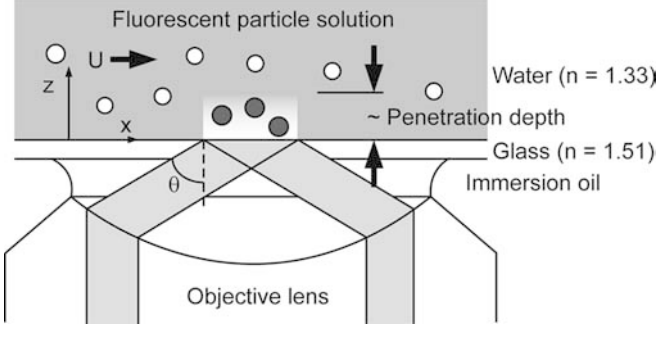

Fig. 1. Schematic of objective-based TIRFM

As mentioned before, the intensity of an evanescent wave decays exponentially with distance z away from the two-media interface (Axelrod et al. 1984):

$$I(z) = I_0 e^{-z/d} \tag{2}$$

where I_0 is the light intensity at the interface and d is known as the evanescent wave penetration depth. The penetration depth, which characterizes the evanescent field, can be calculated as:

$$d = \frac{\lambda_0}{4\pi}\left(n_1^2 \sin^2\theta - n_2^2\right)^{-1/2} \tag{3}$$

where λ_0 is the wavelength of the incident light and n_1 and n_2 are the indices of refraction for glass and water, respectively. Based on these calculations, one can choose the appropriate laser wavelength and microscope objective or prism to achieve the desired penetration depth.

In the present experiment, illustrated in Fig. 2, we have adopted the prismless TIRFM method. A dual-head Quantel Brilliant Q-Switched Nd:YAG laser was used to generate a pair of 532-nm, 5-ns laser pulses to illuminate the flow. The laser heads were timed to fire with a pre-determined pulse separation (1.1 ms to 3.3 ms, depending on shear rate), illuminating two images for use in a PTV analysis. The beams were focused off-axis at the back focal plane of a Nikon PL Apo NA 1.4 100× oil immersion objective lens mounted on a Nikon Eclipse TE200 inverted epi-fluorescent microscope. Because the laser beam is focused off-axis, the beam incident angle at the glass–fluid interface can be controlled by changing the radial location of the laser beam. With water as the sample fluid, the experimental setup had a critical angle of θ_c=61.9°. At incident angles equal to or larger than θ_c, the laser beam could be totally reflected off the water–glass interface, creating an evanescent wave field. With a water–glass interface, λ_0=532 nm and *NA*=1.4, it can be calculated that the penetration depth is approximately 150 nm when the incident angle is θ=63.4°.

The test cell consisted of a precision glass cover slip, on which a polydimethylsiloxane (PDMS) microchannel was attached. The PDMS channels were fabricated using standard *soft lithography* techniques (Duffy et al. 1998) and measured 31±1-μm deep, 250±1-μm wide, and 25-mm long. They were bonded to the test surface after exposure to an oxygen plasma, which renders both the glass and PDMS surfaces highly hydrophilic for a short time, during which they bond on contact. Following bonding, the channels were immersed in deionized water to maintain their hydrophilic surface characteristics.

To create hydrophobic microchannels, it is necessary to coat the glass surface with a transparent and hydrophobic substance because glass is naturally hydrophilic. We coated the glass by immersing it into a 5-mM octadecyltrichorosilane (OTS) solution (dissolved in hexadecane) at room temperature for several hours. A self-assembled monolayer (SAM) of OTS formed on the glass surface, and was made permanent after the glass was rinsed in hexane and ethanol, dried in nitrogen, and baked at 100°C on a hotplate for a few hours. The coating process was performed in a nitrogen gas chamber to avoid bulk

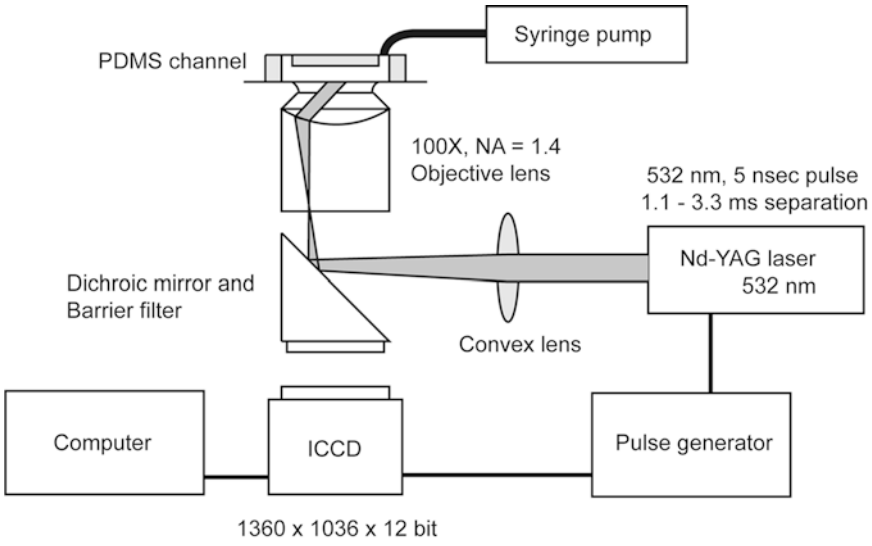

Fig. 2. Schematic of the experimental setup

polymerization. The coated glass was bonded to a cleaned, patterned PDMS channel to create a hydrophobic microchannel. It has been reported that surface roughness can strongly inhibit boundary slip by transferring momentum if liquid molecules are trapped inside the holes of the monolayer (Pit et al. 2000). Thus, an atomic force microscope (AFM) measurement of glass surface roughness was also performed. The polished Pyrex glass wafer was measured to have a surface root mean square (RMS) roughness of 2 nm, while the same wafer had a surface roughness of 4 nm after OTS coating.

Monodisperse Fluorescent Polymer Microspheres (Duke Scientific) with diameters of 200 nm (±5%) and 300 nm (±3%), suspended in pure water at 0.02% and 0.04% volume fractions, respectively, were used as seed particles in this experiment. These microspheres have a peak absorption wavelength of 542 nm and emit a red visible light at 612 nm. Particle solutions were flowed through the test channels using a Harvard Apparatus 22 syringe pump, at flow rates ranging from 0.6 μL/min to 6.0 μL/min (±0.35%). An air gap between the piston and the fluid in the syringe and long tubes were used to dampen pulsations from the syringe motion. Near-wall particle images were projected onto a Q-Imaging Intensified Retiga CCD camera, which has a capacity of recording 1360×1036-pixel 12-bit images. Under 100× magnification, each image pixel corresponds to 64.3 nm in the flow channel and the diffraction-limited spot size is 30.9 μm (Meinhart and Wereley 2003). For 200-nm and 300-nm particles, the image diameters are 36.8 μm and 43.1 μm, respectively (Santiago et al. 1998). Typically, 200 image pairs were recorded for each flow condition. The recorded image pair was finally analyzed with a PTV algorithm written in our group using the MATLAB programming environment. The choice of PTV rather than PIV is an important one, and this will be readdressed later on.

Measurements were taken at several shear rates. For the results presented here, the shear rate was estimated from the applied volume flow rate, Q, assuming steady laminar flow of an incompressible fluid between two parallel plates without wall slip:

$$\dot{\gamma}_{\text{wall}} = \left(\frac{\mathrm{d}u}{\mathrm{d}y}\right)_{\text{wall}} = \frac{6Q}{h^2 w} \tag{4}$$

where h is the channel depth and w is the channel width. If there is significant slip at the wall, the shear rate could be slightly lower than what is estimated here (Choi et al. 2003). However, for the current experiments, any possible slip velocity is so small that this uncertainty can be neglected (this presumption will be confirmed by the results in the following section).

3 Results and discussion

Figure 3 compares particle images of widefield (direct, flood) illumination and evanescent field illumination. A large amount of background noise is observed in the case of direct illumination. Such background noise is attributed to the light emitting from the out-of-focus particles in the bulk of the fluid and such images are common in micro-PIV measurements, but lead to poor cross-correlations during PIV analysis. Evanescent field illumination, on the other hand, eliminates much of the background noise because the evanescent light penetration depth is restricted to approximately 150 nm, and particles in the bulk fluid are not illuminated. This characteristic allows easy detection of only particles that are close to the channel surface.

To measure particle velocities near the channel surface, several hundred image pairs at various low shear rates were taken for subsequent PTV image analysis. Bright particles with intensities above a pre-determined threshold value were identified in each image. In this study, the intensity threshold was set at 50% of the brightest particle intensity (usually about 1,500–2,000 counts from a 12-bit CCD camera). This threshold value allowed us to detect almost every particle which can be identified with the naked eye, and restricts the analysis to particles that are well within the evanescent field and in focus. The number of particles identified in one image is not very sensitive to the exact threshold value. Typically, about 10–20 particles were identified in each image, although approximately

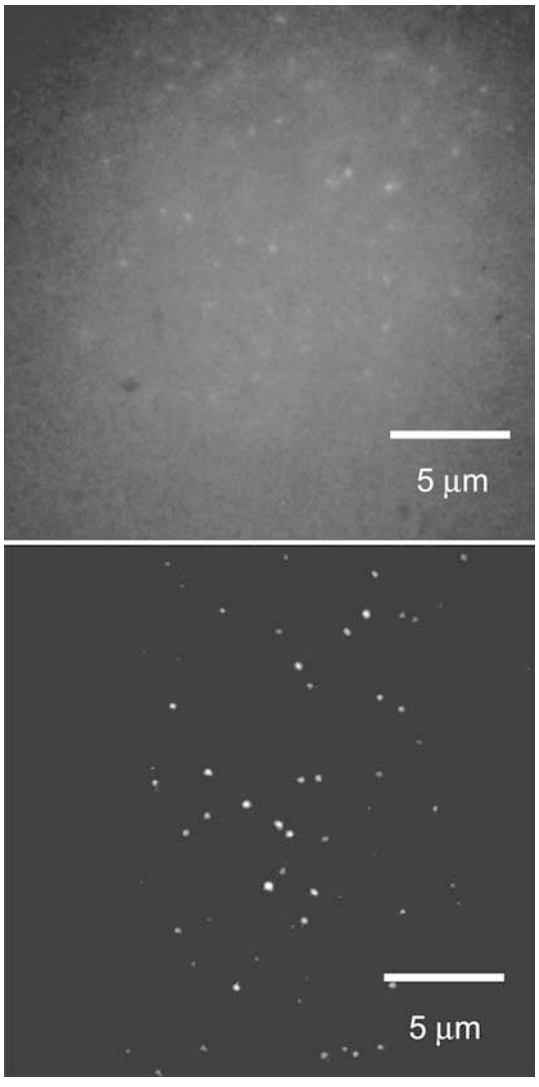

Fig. 3a, b. Particle images of different illumination methods. **a** Widefield (direct, flood) illumination. **b** Near-wall TIRFM image

50% of these were not tracked between images due to out-of-plane diffusion, which causes particles to enter and leave the observation region.

It is important to point out that the determination of an intensity threshold sets an *observation range*, as illustrated in Fig. 4. The lower bound of the observation range is the particle radius, representing a particle in contact with the channel surface. As the particle moves further from the wall, and, hence, into a region of lower illumination intensity, the emitted intensity also falls. Thus, the intensity threshold chosen sets an upper bound on the observation range, which is different from the penetration depth of the evanescent field. The exact size of the observation range was not known in these experiments, and this uncertainty turned out to be the major source of uncertainty in these experiments and is discussed later on.

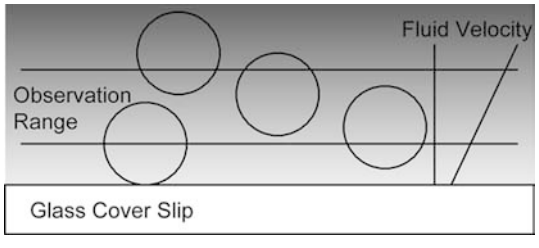

Fig. 4. Schematic of near-wall particles moving near the surface, illustrating the observation range

Although tracking the particle displacements in the x–y plane (parallel to the surface) was straightforward, tracking the particle motion in the z axis (normal to the surface) is not easy. Ovryn (2000) developed a method to determine the three-dimensional position of a spherical particle based on resolving the spatial variations in the scattering pattern. However in the evanescent field, illumination intensity varies exponentially with the distance from the wall (as shown in Eq. 2), and, consequently, it is not easy to directly quantitatively associate the fluorescent scattering of a particle in a nonuniform illumination field with the particle's distance from the wall. For this reason, we did not attempt to track the particle's motion normal to the surface. There is no reason why this should not be possible in the future.

The intensities of pixels surrounding the peak intensity were fitted to a two-dimensional Gaussian curve (Adrian and Yao 1985; Olsen and Adrian 2000; Bourdon et al. 2004). Because the particles are known to be spherical with a diameter standard deviation of less than 5%, a two-dimensional Gaussian curve fit closely approximates the Lommel function and allowed us to locate the particle center coordinates with sub-pixel resolution. Particles were matched between images using a custom particle tracking algorithm and displacement vectors were calculated from the displacements of particle centers. A threshold displacement was imposed to detect error vectors, which were defined as displacements larger than deemed reasonable. These large displacement vectors usually result from matching two different particles mistakenly. At each testing condition, the total number of validated displacement vectors ranged from 700 to 1,500. Using the geometric scale and the applied pulse separa-

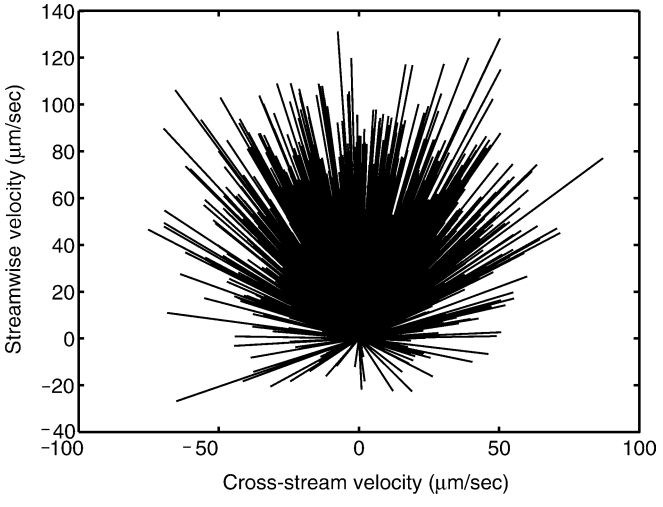

Fig. 5. Distribution of particle velocity vectors of 200-nm particles with $\dot{\gamma} = 469\ \mathrm{s}^{-1}$

tion, a velocity vector can be calculated from each displacement vector. Figure 5 shows an example of a collection of velocity vectors obtained for a single shear rate. The Brownian motion is particularly strong due to the particle's small size.

4 Cross-stream velocity analysis

Analysis of the displacements of particles in the cross-stream direction was used to check the consistency of the experiment results. In this direction, in the absence of any mean flow, one would expect that the particle motion would be purely driven by thermal fluctuations. Indeed, we found that the distributions of spanwise velocities had a Gaussian distribution with mean and skewness close to zero. The width of the particle displacement distribution, σ, was used to compute the local diffusion coefficient, D:

$$D = \frac{\sigma^2 \Delta t}{2} \tag{5}$$

and Fig. 6 shows the cross-stream diffusion coefficient obtained for 200-nm (solid symbol) and 300-nm (open symbol) particles at a variety of different streamwise shear rates over both hydrophilic and hydrophobic surfaces. The diffusion coefficient is scaled by the particle radius, r, and the dotted lines represent scaled particle diffusion in an infinite medium calculated based on the Stokes-Einstein relation:

$$D_0 \cdot r = \frac{k_B T}{6\pi\eta} \tag{6}$$

where D_0 is the Stokes-Einstein diffusion coefficient, k_B is the Boltzmann constant, T is the medium temperature, and η is the fluid viscosity. As expected, the measured spanwise diffusion coefficients are independent of the streamwise shear rate and the diffusion coefficient, when appropriately scaled, is independent of the particle radius.

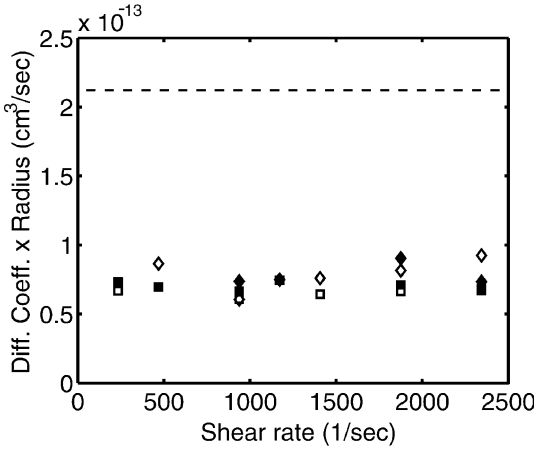

Fig. 6. Cross-stream Brownian motion of particles in an infinite medium and near-wall (experiment). *Solid* symbols represent 200-nm particles and *open* symbols represent 300-nm particles (*squares*=hydrophilic surface; *diamonds*=hydrophobic surface). The *dashed line* denotes particle diffusion in an infinite medium calculated on the basis of the Stokes-Einstein relation

However, as indicated by the dotted line in Fig. 6, the measured values for D are approximately 30% that of the bulk diffusion expected. This is confirmation of the presence of hindered diffusion of particles near a solid surface (Goldman et al. 1967a, 1967b). If we use the observed value of D with the theory for hindered diffusion (Goldman et al. 1967a, 1967b) to calculate the "apparent particle distance" from the wall, defined as the distance between the particle center and the wall, we find it to be 110 nm for the 200-nm particles and 165 nm for the 300-nm particles. This is consistent with the high intensity threshold chosen, which defines a small observation range. Unfortunately, since we did not carefully monitor the observation range, a more precise estimate is not available for this data.

5 Streamwise velocity analysis

Figure 7 shows an example of the distribution of the streamwise velocities, found by projecting the velocity distributions onto the mean flow direction. Several features are worth noting. Firstly, the location of the peak of the distribution increases with increasing shear rate, as one would expect. Less expected, and in contrast to the distributions for the spanwise velocities, is the observation that the distribution widens with increasing shear rate, and that the skewness clearly shifts from 0.15 at the low shear rate (barely noticeable) to a clearly observable positive value of 0.85 (a stronger positive tail) at the highest shear rate presented. In this case, the most probable velocity is quite different from the average velocity, raising a fundamental question about the definition of the actual *fluid* velocity in terms of the observed *particle* velocity distribution. Figure 8 shows the variation of the mean velocities as a function of shear rate; the error bars depict the standard deviation about the mean. The velocities fall on a straight line through the origin, and there are no discernible differences between the hydrophilic and hydrophobic surfaces and, more interestingly, between the 200-nm and 300-nm diameter particles.

The reason for the observed increase in the distribution width and skewness can be explained in terms of the observation range from which the particle motions are

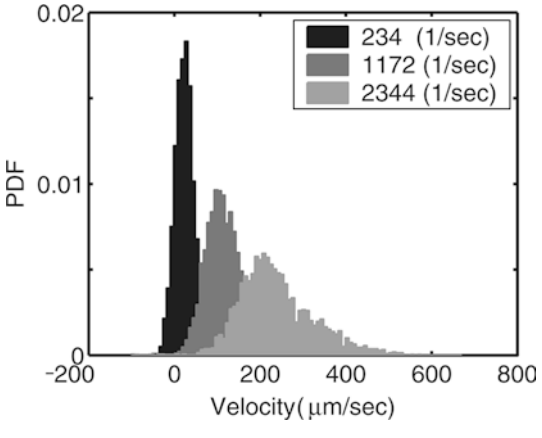

Fig. 7. Experimentally measured distribution of streamwise velocities of 200-nm diameter particles over a range of shear rates

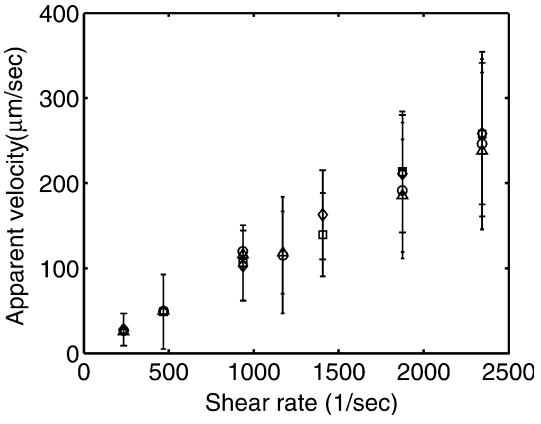

Fig. 8. Apparent particle velocity vs. shear rate (*diamonds*=300-nm particle, hydrophilic surface; *squares*=300-nm particle, hydrophobic surface; *triangles*=200-nm particle, hydrophilic surface; *circles*=200-nm particle, hydrophobic surface)

recorded. At each shear plane, the true velocity distribution for tracer particles has a Gaussian shape with a mean equal to the flow velocity at that plane, and standard deviation determined by the temperature and particle size. However, any micro-PTV or PIV system, including the current TIRV method, integrates through the observation range and, thus, samples particle motion from a range of shear planes over which the mean velocity changes. Thus, for a fixed observation range, the range of mean velocities sampled increases as the shear rate increases, leading to the observed broadening of the velocity distribution for the streamwise velocity. A similar argument can be used to explain the increasing skewness at higher shear rates. Here, we note that, due to the presence of the wall, a particle is more likely to move upwards (and, thus, experience a higher local velocity) than to move downwards (and experience a lower local velocity). Thus, higher velocity fluctuations are more probable than lower ones in the vicinity near the wall (a similar argument is used to explain positive skewness in the streamwise velocity distribution in a turbulent wall-bounded flow).

The lack of any differences between the mean velocities obtained for 200-nm and 300-nm particles is more troubling. One would expect that the 300-nm particles would sample shear planes at higher local velocities than those sampled by the 200-nm particles, and, thus, the average velocities should be larger for the larger tracer particles. The fact that this is not observed remains a somewhat puzzling result and one that needs to be resolved in future measurements. However, there are several factors that are not yet well understood, but which could contribute to this counter-intuitive observation, including uncertainty in the measurement of the illumination observation range, particle motions in addition to pure translation (such as rolling motion), and other forces on the particles (e.g., colloidal).

The drift velocities measured can result from two effects: (1) the finite thickness of the observation range and (2) the possible existence of a slip velocity at the surface. We can assess the relative contributions of these effects using a very simple theoretical model. If we assume a constant shear very near the surface, we can write the local velocity profile as:

$$u(y) = u_s + \dot{\gamma} y \tag{7}$$

where u_s is the slip velocity. If we use a Navier representation for the slip velocity, $u_s = l^* \dot{\gamma}$, (where l^* is the slip length) and compute the average velocity in the mean depth of the observation range, δ, we find that the average, or "apparent slip" velocity is:

$$\bar{u} = (l^* + \delta)\dot{\gamma} \tag{8}$$

The slope of the data in Fig. 8 is approximately 100 nm, representing this combination of both the penetration depth and the slip length. Given that the observation range is estimated to be approximately 100–150 nm, this suggests that the slip length, if present, is likely to be no more than 10 nm, which is consistent with the results of Choi et al. (2003) for these low shear rates. At the present moment, our lack of quantitative knowledge about the evanescent wave penetration depth (which probably varied from experiment to experiment) and the observation range makes a more precise estimate for the slip length impossible at this time. However, with the appropriate characterization and consistent control of the observation range, this measurement will be possible and such experiments are currently underway. Finally, we note that a slip length of order 1,000 nm (as proposed by Tretheway and Meinhart 2002, and Zhu and Granick 2002) is completely unsupported by these data, as it would predict apparent slip velocities at least an order of magnitude larger than observed, and would be independent of any reasonable estimate for the observation range.

6
Comparison with numerical simulation

The experimental results were compared with a numerical simulation of near-wall Brownian motion in shear flow. The motivation for this was to generate an intuitive model with which to help understand the experimental results. This simple two-dimensional numerical model was developed to simulate the Brownian motion of particles with radius, r, in a no-slip steady-state Poiseuille flow between parallel infinite plates separated by a distance h, the experimental channel depth. At the beginning of the simulation, 10,000 particles were uniformly distributed between r and Δ, the assumed upper bound of the observation range. At each time step, each particle was moved by a linear combination of the mean shear flow (evaluated at the particle's geometric center) and Brownian motion (sampled from a normal distribution with a zero mean and a standard deviation of $(2D\Delta t)^{1/2}$). Other effects, such as particle rotation, etc., were not considered at this time.

The Brownian motion was modified to account for the hindered diffusion both parallel and perpendicular to the wall (Brenner 1961; Goldman et al. 1967a, 1967b). For the Brownian motion normal to the wall (Brenner 1961), the modified diffusion constant $D_\perp$ is such that:

$$\frac{D_\perp}{D_0} = \left\{\frac{4}{3}\sinh\alpha\sum_{n=1}^{\infty}\frac{n(n+1)}{(2n-1)(2n+3)}\right.$$

$$\left.\times\left[\frac{2\sinh(2n+1)\alpha+(2n+1)\sinh 2\alpha}{4\sinh^2\left(n+\frac{1}{2}\right)\alpha-(2n+1)^2\sinh^2\alpha}-1\right]\right\}^{-1} \tag{9}$$

where D_0 is the Stokes-Einstein diffusion coefficient, $\alpha=\cosh^{-1}(z/r)$, and z is the distance between the geometrical center of a particle and the wall. For the Brownian motion parallel to the wall, the modified diffusion constant is such that:

$$\frac{D_\parallel}{D_0} = 1-\frac{9}{16}\left(\frac{r}{z}\right)+\frac{1}{8}\left(\frac{r}{z}\right)^3-\frac{45}{256}\left(\frac{r}{z}\right)^4-\frac{1}{16}\left(\frac{r}{z}\right)^5+O\left(\frac{r}{z}\right)^6 \tag{10}$$

by the method of reflection (Goldman et al. 1967a) for $(z-r)/r>1$, and:

$$\frac{D_\parallel}{D_0} = -\frac{2\left[\ln\left(\frac{z-r}{r}\right)-0.9543\right]}{\left\{\ln\left(\frac{z-r}{r}\right)\right\}^2-4.325\ln\left(\frac{z-r}{r}\right)+1.591} \tag{11}$$

which is the asymptotic solution (Goldman et al. 1967b) for $(z-r)/r<1$.

After 1,000 time steps, particles that remained within the observation range were counted and their displacements from their initial positions were calculated to obtain a particle displacement distribution, similar to that obtained in the physical experiments. To emulate the experiment, plate separation distance, particle radii, flow shear rate, and the total time (1,000 time steps) were chosen to be equal to measurement conditions, and the assumed observation range was chosen to be 100–175 nm from the wall.

Problems can arise when the simulated particle is predicted to pass through the solid surface during the finite time step. In the present simulation, two different wall boundary conditions were tested to deal with this situation. The first condition applied a specular reflection, in which the particle was simply reflected off the wall and back into the flow. The second condition emulated a near-wall lubrication condition and simply allowed the particle to remain at the wall until Brownian motion perpendicular to the wall transported it back into the bulk flow, one or more time steps later. Only a few particles needed to be treated with these heuristic boundary conditions, and it was found that the two models gave almost indistinguishable results, with less than 1% statistical difference in the mean and standard deviation of the resultant particle distributions. Figure 9 shows the streamwise velocity distributions of 200-nm particles at various shear rates, while Fig. 10 shows the variation of the mean velocities and their standard deviations, denoted as error bars, as a function of shear rate. The rather simplistic nature of the simulation is such that one should not make direct, quantitative, comparisons with the experimental results (Figs. 7 and 8). In addition, the choice of observation range for the computation has not yet been optimized to match the simulation results with those of the experiments. Nevertheless, the similarities between the two figures are striking, showing similar increases in the mean, standard deviation, and (less obvious, but present) skewness of the distributions as the shear rate increases.

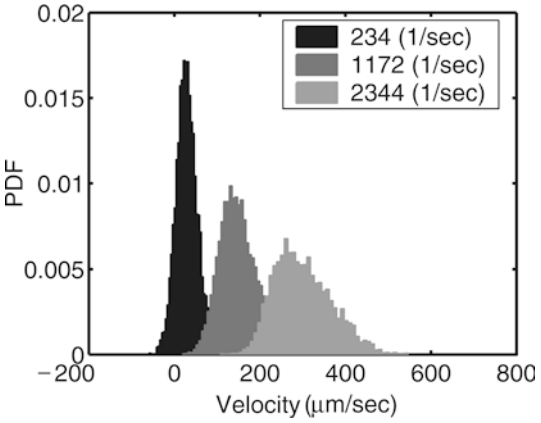

Fig. 9. Streamwise velocity distribution of 200-nm particles determined from a Monte Carlo simulation at an observation depth of 175 nm

Unlike the experimental results in Fig. 8, which did not show any difference in measuring velocity using different particle sizes, there is a clear difference in the estimated velocity using different particle sizes in Fig. 10. As discussed earlier, this difference due to particle size is to be expected for a fixed observation range, and this result adds weight to our suspicion that the observation range in the experiments were not consistent, and that future experiments should pay more attention to this important issue.

7 Concluding remarks

We have demonstrated that the total internal reflection velocimetry (TIRV) method can be a very powerful

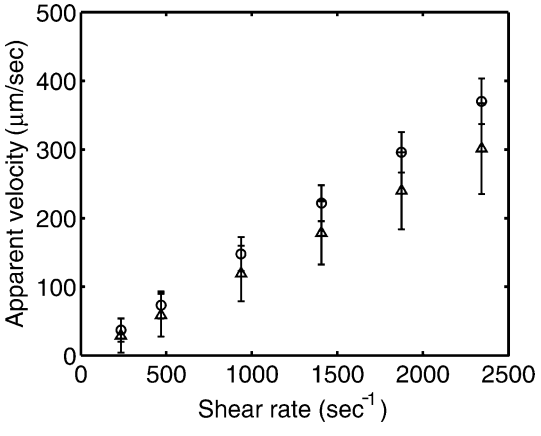

Fig. 10. Streamwise apparent velocity predicted by simulation (*triangles*=200-nm particles; *circles*=300-nm particles) at an observation depth of 175 nm

technique for the study of near-wall flows in microfluidic systems. TIRV images have very low background noise that allows accurate PIV and PTV measurements of flow velocities within a few hundred nanometers of the surface. By using sub-micron seed particles, we have demonstrated the ability to measure both velocity distributions and mean velocities in the plane parallel to the surface.

The determination of velocities in the streamwise and spanwise directions is extremely accurate, comparable to "standard" micro-PIV techniques, but is limited by the same constraints—the accuracy of particle centroid location, diffraction-limited imaging of sub-micron particles, etc. (Meinhart and Wereley 2003). However, the technique also promises the ability to use intensity information to obtain wall-normal displacements, as well as precise estimates for the slip velocity at the surface. The present implementation did not (unfortunately) control with sufficient accuracy or consistency the characteristics of the evanescent wave penetration depth, which is very dependent on the incident beam angle. For this reason, we were not able to measure vertical particle motion and our current resolution of the slip length measurement is limited such that we can only state that a slip length, if present, is of the order of 10 nm or less. However, the estimate for the slip length is limited only by the accuracy with which we can measure the observation range, and so, we expect to be able to make measurements with uncertainties of less than 5 nm in the near future.

The accuracy of the TIRV system can still be improved by several means that are subject to future investigation. First, by using a shorter illumination wavelength, the penetration depth of the evanescent field can be decreased. Secondly, smaller seed particles can move closer to the channel surface than larger particles, although they also suffer from higher Brownian diffusion, and so, the particle drop-out will increase. Both changes will allow direct measurements of flow velocities that are closer to the channel surface, where slip might contribute more significantly to the local flow velocity.

Finally, and most importantly, the technique does raise fundamental questions regarding the use of "passive" tracer particles to estimate the velocity field in microfluidic systems. Our results reveal several features of particle motion in the near vicinity of the surface, including non-Gaussian Brownian motion (due to the finite thickness of the observation range) and hindered diffusion due to near-wall lubrication effects. There are also effects other than the translational hydrodynamic drag that can contribute to the particle motion such that the velocity measurements might be compromised. One is the possibility of particle rotation; a second is the possibility of particle–wall colloidal interactions and the relative roles of gravity, thermal noise, and electrostatic effects (both the bead and the surface have surface charges). This is an area that has been studied by a number of researchers, including Flicker et al. (1993), Crocker and Grier (1996), and Behrens and Grier (2001), who have identified colloidal forces that are highly dependant on bead diameter, surface charge, ionic strength (and for pure water such as that used in these experiments, the rate at which ions leak from the glass into solution). A full treatment of these issues is beyond the scope of the current paper, and indeed, the experimental techniques described here can be used in further studies of such phenomena. Perhaps the most important consequence of this is that techniques that treat *ensembles* of particles (such as PIV, which looks at the collective motion of particles in an interrogation region, and often averages cross-correlations before peak detection) might be suspect close to walls due to particle interference effects which cannot be neglected and where the particle motion is not represented by Gaussian statistics (and, hence, the average particle velocity is different from the most probable particle velocity). For this reason, tracking each particle independently and then computing statistics from the individual particle motions might yield a more accurate view of the near-wall velocity field.

References

Adrian RJ, Yao CS (1985) Pulsed laser technique application to liquid and gaseous flows and the scattering power of seed materials. Appl Optics 24:44–52

Axelrod D, Burghardt TP, Thompson NL (1984) Total internal reflection fluorescence (in biophysics). Annu Rev Biophys Bioeng 13:247–268

Barrat JL, Bocquet L (1999) Large slip effect at a nonwetting fluid-solid interface. Phys Rev Lett 82(23):4671–4674

Behrens SH, Grier DG (2001) The pair interaction of charged colloidal spheres near a charged wall. Phys Rev E 64:050401

Bourdon CJ, Olsen MG, Gorby AD (2004) Validation of an analytical solution for depth of correlation in microscopic particle image velocimetry. Meas Sci Technol 15:318–327

Brenner H (1961) The slow motion of a sphere through a viscous fluid towards a plane surface. Chem Eng Sci 19:242–251

Burmeister JS, Olivier LA, Reichert WM, Truskey GA (1998) Application of total internal reflection fluorescence microscopy to study cell adhesion to biomaterials. Biomaterials 19:307–325

Choi CH, Westin KJA, Breuer KS (2003) Apparent slip flows in hydrophilic and hydrophobic microchannels. Phys Fluids 15(10):2897–2902

Churaev NV, Sobolev VD, Somov AN (1984) Slippage of liquids over lyophobic solid surfaces. J Colloid Interf Sci 97(2):574–581

Cieplak M, Koplik J, Banavar JR (2001) Boundary conditions at a fluid–solid interface. Phys Rev Lett 86(5):803–806

Crocker JC, Grier DG (1996) When like charges attract: the effects of geometrical confinement on long-range colloidal interactions. Phys Rev Lett 77(9):1897–1900

Duffy DC, McDonald JC, Schueller OJA, Whitesides GM (1998) Rapid prototyping of microfluidic systems in poly(dimethylsiloxane). Anal Chem 70:4974–4984

Flicker SG, Tipa JL, Bike SG (1993) Quantifying double-layer repulsion between a colloidal sphere and a glass plate using total internal reflection microscopy. J Colloid Interf Sci 158:317–325

Goldman AJ, Cox RG, Brenner H (1967a) Slow viscous motion of a sphere parallel to a plane wall—I motion through a quiescent fluid. Chem Eng Sci 22:637–651

Goldman AJ, Cox RG, Brenner H (1967b) Slow viscous motion of a sphere parallel to a plane wall—II Couette flow. Chem Eng Sci 22:653–660

Meinhart CD, Wereley ST (2003) The theory of diffraction-limited resolution in microparticle image velocimetry. Meas Sci Technol 14:1047–1053

Olsen MG, Adrian RJ (2000) Out-of-focus effects on particle image visibility and correlation in microscopic particle image velocimetry. Exp Fluids 29:S166-S174

Ovryn B (2000) Three-dimensional forward scattering particle image velocimetry applied to a microscopic field-of-view. Exp Fluids 29:S175-S184
Pit R, Hervet H, Leger L (2000) Direct experimental evidence of slip in hexadecane: solid interfaces. Phys Rev Lett 85(5):980–983
Santiago JG, Wereley ST, Meinhart CD, Beebe DJ, Adrian RJ (1998) A particle image velocimetry system for microfluidics. Exp Fluids 25:316–319
Schnell E (1956) Slippage of water over nonwettable surfaces. J Appl Phys 27(10):1149–1152
Thompson NL, Langerholm BC (1997) Total internal reflection fluorescence: applications in cellular biophysics. Curr Opin Biotech 8:58–64
Thompson PA, Troian SM (1997) A general boundary condition for liquid flow at solid surfaces. Nature 389:360–362
Toomre D, Manstein DJ (2001) Lighting up the cell surface with evanescent wave microscopy. Trends Cell Biol 11:298–303
Tretheway DC, Meinhart CD (2002) Apparent fluid slip at hydrophobic microchannel walls. Phys Fluids 14(3):L9-L12
Watanabe K, Udagawa Y, Udagawa H (1999) Drag reduction of Newtonian fluid in a circular pipe with a highly water-repellent wall. J Fluid Mech 381:225–238
Yamada J (1999) Evanescent wave Doppler velocimetry for a wall's near field. Appl Phys Lett 75:1805–1806
Zettner CM, Yoda M (2003) Particle velocity field measurements in a near-wall flow using evanescent wave illumination. Exp Fluids 34(1):115–121
Zhu Y, Granick S (2002) Limits of the hydrodynamic no-slip boundary condition. Phys Rev Lett 88:106102